ANNALS OF THE NEW YORK ACADEMY OF SCIENCES

Original Article

Morphology control in crystalline nanoparticle–polymer aggregates

Tong Bian and Rafal Klajn

Department of Molecular Chemistry and Materials Science, Weizmann Institute of Science, Rehovot, Israel

Address for correspondence: Rafal Klajn, Ph.D., Department of Molecular Chemistry and Materials Science, Weizmann Institute of Science, 234 Herzl St., Rehovot 76100, Israel. rafal.klajn@weizmann.ac.il

Self-assembly of nanoparticles can be mediated by polymers, but has so far led almost exclusively to nanoparticle aggregates that are amorphous. Here, we employed Coulombic interactions to generate a range of composite materials from mixtures of charged nanoparticles and oppositely charged polymers. The assembly behavior of these nanoparticle/polymer composites depends on their order of addition: polymers added to nanoparticles give rise to stable aggregates, but nanoparticles added to polymers disassemble the initially formed aggregates. The amorphous aggregates were transformed into crystalline ones by transiently increasing the ionic strength of the solution. The morphology of the resulting crystals depended on the length of the polymer: short polymer chains mediated the self-assembly of nanoparticles into strongly faceted crystals, whereas long chains led to pseudospherical nanoparticle/polymer assemblies, within which the crystalline order of nanoparticles was retained.

Keywords: self-assembly; electrostatic; nanoparticles; polymers

Introduction

Assembling inorganic nanoparticles (NPs) into higher-order structures is important for harnessing their unique physicochemical properties and fabricating functional materials of macroscopic dimensions.[1–4] NPs can be organized into ordered structures by solvent evaporation,[5,6] by adding NPs exhibiting complementary surface chemistry,[7,8] or by exposing them to various external stimuli,[9] including light,[10–12] heat,[13,14] magnetic fields,[15,16] redox agents,[17] metal ions,[18,19] acids/bases,[20] gases,[21,22] and other chemical agents.[23] Among them, polymers are particularly interesting owing to their structural and chemical diversity and beneficial mechanical properties, which can be transferred to the resulting polymer–NP composite materials.[24–27] In a pioneering report,[28] Rotello and coworkers used a polymer exhibiting multiple diaminotriazine (DAT) groups to mediate the self-assembly of Au NPs decorated with thymine residues, which form strong hydrogen bonds with and are complementary to the DAT moieties.[28,29] In another notable example, Torii *et al.* reported the coassembly of oligo(ethylene glycol)-coated NPs and poly(acrylic acid) (PAA) into aggregates that exhibited pH-responsiveness; addition of a base induced the deprotonation of PAA, thus eliminating the attractive hydrogen-bonding interactions between the polymer and the NPs.[30] At a low pH, the aggregates could be regenerated, and the assembly–disassembly process could be repeated for multiple cycles. A variety of polymer–NP hybrid materials have also been fabricated by the electrostatic self-assembly of charged NPs with oppositely charged biomacromolecules, including peptides,[31] proteins,[32–34] and DNA.[35–37] Furthermore, much effort has been devoted to organizing (e.g., via hydrogen bonding[38] and hydrophobic interactions[39,40]) inorganic NPs (including anisotropic ones[41]) onto specific domains of phase-segregated block copolymer scaffolds,[42–51] and to assembling NPs

via the layer-by-layer approach.[52–57] However, it is challenging to induce a regular (crystalline) order of NPs by means of polymer-mediated self-assembly, in particular using linear polymers—in fact, nearly all of the above assemblies exhibit random packing of NPs. Although templating NPs into crystalline assemblies has successfully been achieved using globular biomacromolecules,[32,33] it is highly demanding for linear polymer chains to fold so as to assemble NPs in an organized fashion.

Recently, we reported a new method to mediate the self-assembly of charged NPs—that is, NPs functionalized with a monolayer of thiols terminated with charged groups—into high-quality colloidal crystals using oppositely charged small molecules.[58] Our method is based on the finding that attractive Coulombic interactions in water exist between positively charged NPs and anions having three or more negative charges, resulting in amorphous NP/oligoion aggregates; the same is true for negatively charged NPs and small-molecule cations having at least three positive charges. We found that the addition of a volatile salt (such as ammonium carbonate) temporarily increases the ionic strength of the solution, thus disassembling the initial amorphous aggregates; the subsequent evaporation of the salt reestablishes attractive interactions, leading to highly crystalline NP assemblies.[58]

Here, we show that attractive Coulombic interactions also exist between charged NPs and oppositely charged polyelectrolytes (charged polymers), which can thus mediate NP–NP interactions. Remarkably, decreasing the ionic strength of colloidally stable solutions containing charged NPs and oppositely charged polymers resulted in polymer/NP assemblies in which NPs exhibited a crystalline order. Interestingly, the crystalline nature of the resulting assemblies was found for all polymer lengths investigated. At the same time, the average length of the polymer chain had a profound effect on the morphology of the colloidal crystal: the longer the polymer, the less faceted the crystals.

Results and discussion

We worked with monodisperse gold NPs with sizes ranging from ~4.2 to ~7.6 nm and with size dispersity <10%, prepared by reducing $HAuCl_4$ with $t\text{-BuNH}_2\cdot BH_3$ in the presence of oleylamine (OLA).[59] To render the OLA-capped NPs pos-

itively charged, they were subjected to a ligand exchange reaction with (11-mercaptoundecyl)-N,N,N-trimethylammonium bromide (TMA in Fig. 1A; a 10-fold excess). Interestingly, we found that the resulting NPs could not be fully dispersed in water, probably due to an incomplete removal of OLA from the NPs (we hypothesize that a small amount of OLA remains on the NPs to prevent unfavorable contacts between the like-charged TMA head groups). Therefore, a small amount (10 mol%) of a short, electrically neutral thiol (1-hexanethiol, HT) was included during the ligand exchange reaction; unlike OLA, HT is shorter than TMA and can thus screen the electrostatic repulsion between TMAs without compromising the NPs' solubility in water. Nuclear magnetic resonance (NMR) analysis of the monolayer on the resulting NPs revealed the presence of ~77% TMA and ~23% HT, indicating the preferential adsorption of HT on the NPs (feed ratio, TMA/HT = 9:1), again probably due to the unfavorable TMA–TMA contacts.

When TMA-functionalized NPs (Au·TMA) dispersed in water were mixed with an aqueous solution of PAA, they rapidly aggregated. The resulting aggregates were amorphous, irrespective of the order of the addition (Fig. 1A) or the length of PAA (we worked with PAA with three different degrees of polymerization: $M_w \approx 1800$, $M_w \approx 100k$, and $M_v \approx 450k$, denoted as PAA_{1800}, PAA_{100k}, and PAA_{450k}, respectively; Materials and methods, online only). To study the aggregation process in more detail, we titrated solutions of Au·TMA with PAA (Fig. 1B and C) and vice versa (Fig. 1D and E). To ensure a high degree of PAA deprotonation, the pH values of both the titrant and the titrated solution were set to 11. Figure 1B shows the dependence of the wavelength of maximum absorbance, λ_{SPR} (due to NPs' surface plasmon resonance (SPR); proportional to the degree of aggregation[60,61]) as a function of the amount of PAA added. For all the PAAs, λ_{SPR} increased until it reached a maximum at ~540 nm, followed by a slight decrease. The degree of decrease in λ_{SPR} upon continued titration was the highest for PAA_{450k} (Fig. 1B, gray markers), which can be attributed to the ability of the longest polymer to most efficiently (yet still partially) break the initial Au·TMA/PAA aggregates, since the continuously added PAA tends to maximize the contact with the oppositely charged Au·TMA. It is worth noting that, owing to its high average molecular
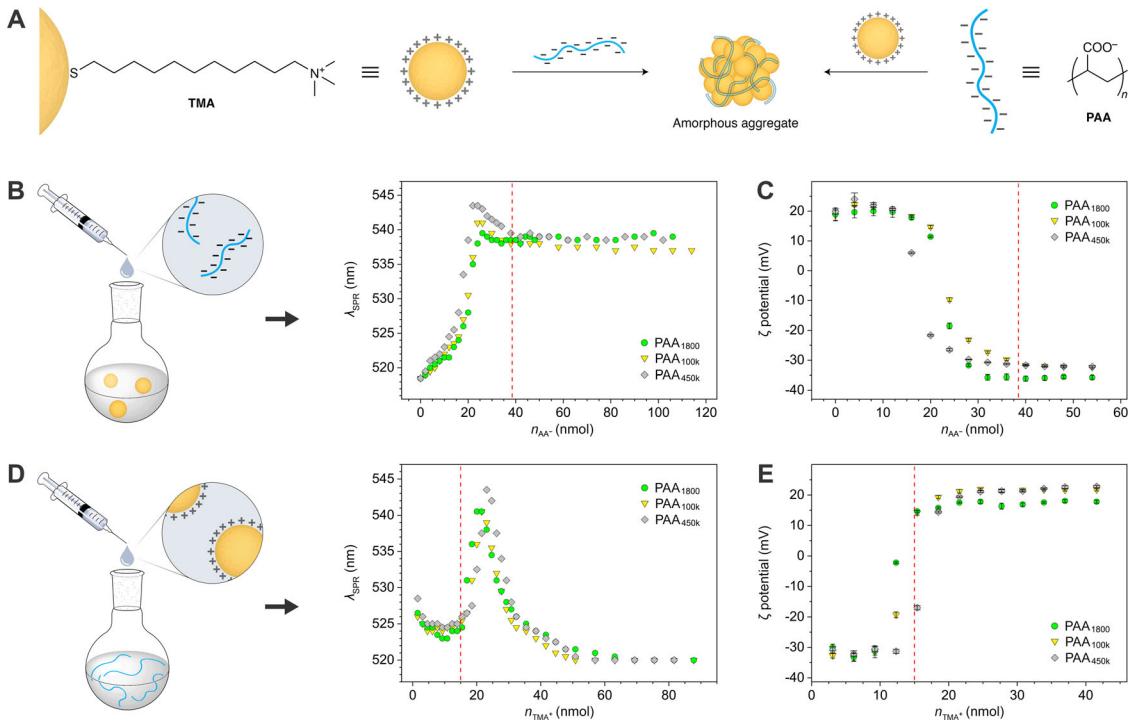
Figure 1. Aggregation of positively charged nanoparticles with polyanions. (A) Structural formulas of (11-mercaptoundecyl)-N,N,N-trimethylammonium (TMA; counterion, Br$^-$) and deprotonated poly(acrylic acid) (PAA), and preparation of amorphous NP aggregates by treating Au·TMA with PAA (left) and PAA with Au·TMA (right). (B) Changes in the position of the Au·TMA's surface plasmon resonance (SPR) peak as a function of the amount of PAA added. The titrated solution contained 38.5 nmol of the NP-bound TMA groups. The amount of titrant added is expressed in terms of the number of acrylic acid (AA) repeating units. (C) Changes in the ζ potential of Au·TMA solution as a function of the amount of PAA added in the same titration as in panel B. The dashed red lines in panels B and C denote the theoretical point of neutrality (i.e., the number of TMA groups equalized by the number of AA units added). (D) Changes in the position of the Au·TMA's SPR peak as a function of the amount of Au·TMA added to the solution of PAA. The titrated solution contained a total of 15 nmol of the AA repeating units. The amount of titrant added is expressed in terms of the number of NP-bound TMA groups. (E) Changes in the ζ potential of PAA solution as a function of the amount of Au·TMA added in the same titration as in panel D. The dashed red lines in panels D and E denote the theoretical point of neutrality (i.e., the number of AA units equalized by the number of NP-bound TMA groups added). The Au·TMA used in the titrations had a diameter of 6.34 ± 0.57 nm.

weight, PAA$_{450k}$ contains ∼10 times more COO$^-$ groups than the number of NMe$_3^+$ groups per single NP. By contrast, PAA$_{1800}$ contains only ∼25 repeating units (compared with ∼600 TMAs per NP) and thus behaves similarly to small negatively charged molecules, which are incapable of disassembling the initially formed Au·TMA/oligoanion aggregates.[58]

It is interesting to point out that the maximum in the λ_{SPR} versus n_{AA} plot (Fig. 1B) does not overlap with the electroneutrality point (defined as the volume of added PAA solution such that the number of acrylate units corresponds to the number of NP-bound TMA groups). Specifically, the highest value of λ_{SPR} was reached at ∼60% the expected

amount of PAA added (Fig. 1B). To obtain further insight into these results, we followed the titration process by monitoring the ζ potential of the solution (Fig. 1C). At the early stage of the titration, the ζ potential remained roughly constant at ∼20 mV, which, together with the steadily increasing λ_{SPR} (Fig. 1B), can be explained by the formation of increasingly larger aggregates within which PAA is trapped between the NPs (and thus does not contribute to the surface charge). Then, the ζ potential dropped to and stabilized at approximately –30 mV (Fig. 1C), indicating a transition from positively into negatively charged aggregates. Similar to the UV/Vis titration, this transition occurred much
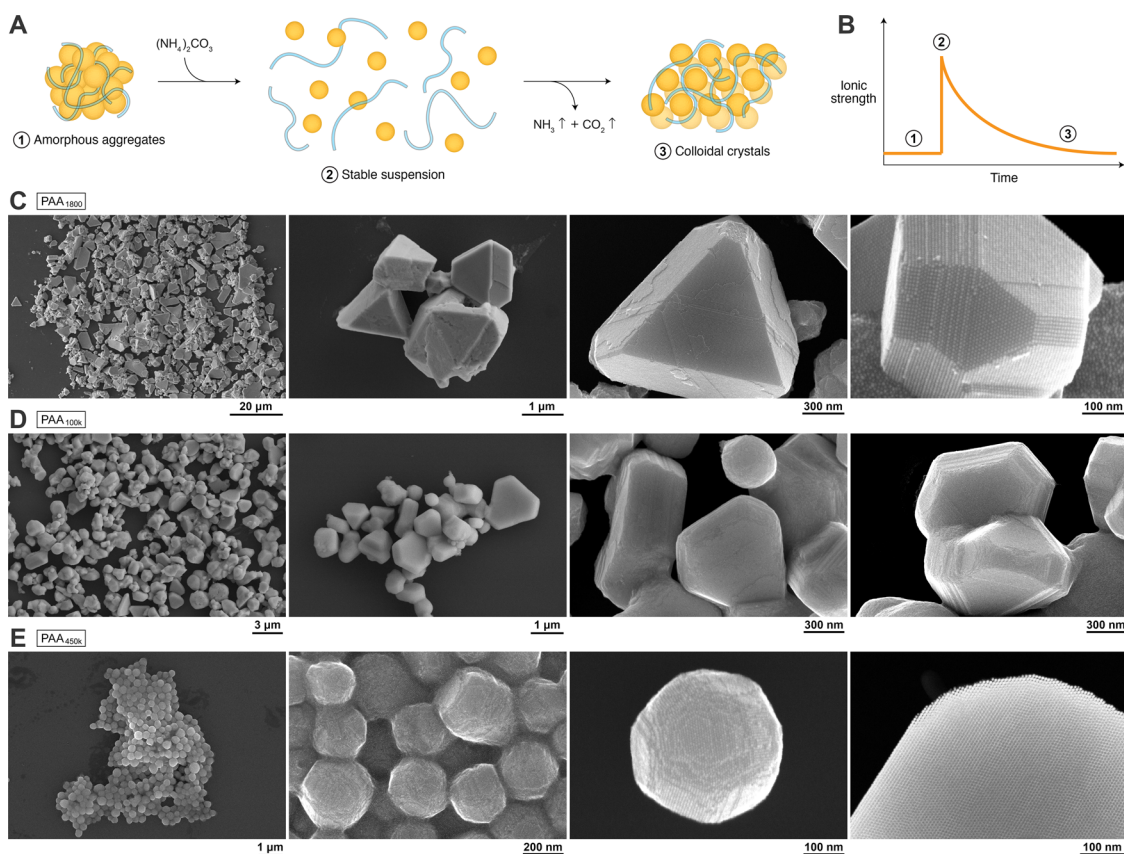
Figure 2. Crystalline assemblies of TMA-coated Au NPs and PAA. (A) Strategy devised to transform amorphous aggregates of Au·TMA and PAA into crystalline ones. (B) Schematic illustration of changes in the ionic strength at different stages of the process. (C) Scanning electron microscopy (SEM) images of crystalline assemblies obtained from Au·TMA and the shortest PAA (PAA$_{1800}$). NP diameters, from the left: 4.84 ± 0.37 nm; 4.84 ± 0.37 nm; 7.57 ± 0.54 nm; 7.57 ± 0.54 nm. (D) SEM images of crystalline assemblies obtained from Au·TMA and medium-sized PAA (PAA$_{100k}$). NP diameters, from the left: 6.34 ± 0.57 nm; 6.34 ± 0.57 nm; 6.34 ± 0.57 nm; 4.93 ± 0.44 nm. (E) SEM images and (right) a high-angle annular dark-field scanning transmission electron microscopy (HAADF-STEM) image of crystalline assemblies obtained from Au·TMA and the longest PAA (PAA$_{450k}$) (see also Fig. S1, online only, for sideview SEM images). NP diameters, from the left: 5.07 ± 0.41 nm; 5.07 ± 0.41 nm; 5.07 ± 0.41 nm; 6.34 ± 0.57 nm.

earlier than expected based on the electroneutrality condition. We attribute this behavior to the high conformational flexibility of the polymers, which renders the COO$^-$ groups more available for intermolecular interactions than the oppositely charged NMe$_3^+$ groups residing on and being constrained by the "hard" NP scaffolds.

Interestingly, a different behavior was observed upon reversing the order of titration. Specifically, the initial sharp increase in λ_{SPR} was followed by its precipitous decrease, ultimately resulting in a low value of λ_{SPR} characteristic of free Au NPs (Fig. 1D). This result indicates that upon continued addition, Au·TMA—unlike PAA (Fig. 1B)—

can quantitatively disassemble the initially formed NP/polymer aggregates. This result is interesting, given that the charge density on Au·TMA and PAA is similar; apparently, it is the morphology of the polyion (spherical NP versus linear polymer) that plays the key role. Concurrent ζ potential titrations revealed that the solutes' surface charge initially remained constant at approximately −30 mV, indicating that Au·TMA added at the early stage of the titration became wrapped around the PAA chains (present in excess). Then, a rapid transition to ζ ≈ +20 mV was observed near the electroneutrality point, confirming the results of the UV/Vis titrations.
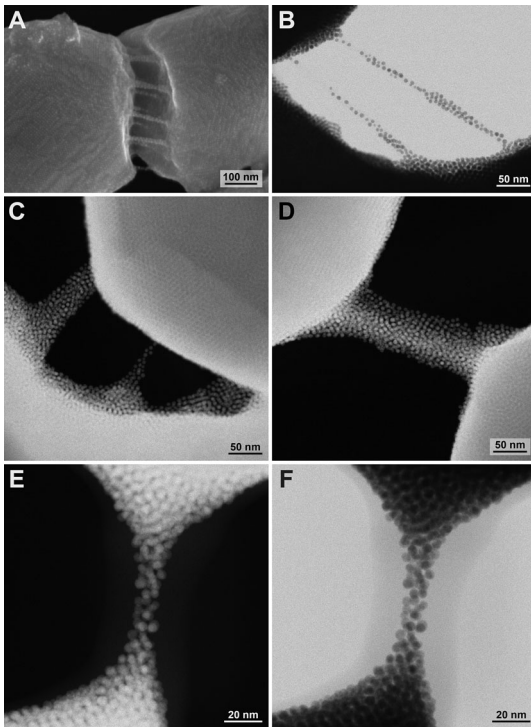
Figure 3. High-resolution SEM (A), bright-field STEM (BF-STEM) (B and F), and HAADF-STEM (C–E) images of Au·TMA/PAA$_{450k}$ aggregates, focusing on the boundaries between neighboring aggregates. The images in panels E and F show the same region, imaged by HAADF-STEM and BF-STEM, respectively. The aggregates were prepared from 6.34 ± 0.57 nm Au·TMA.

We have previously demonstrated[58] that amorphous Au·TMA/oligoanion aggregates can be transformed into crystalline ones by increasing the ionic strength of the solution (thus screening the electrostatic interactions between the NPs and small-molecule ions), followed by decreasing the ionic strength in a controllable manner, for example, by evaporating volatile salts (such as ammonium carbonate; Fig. 2A and B). Here, we found that adding a concentrated solution of $(NH_4)_2CO_3$ could effectively eliminate attractive interactions between Au·TMA and PAA, irrespective of the polymer's chain length, affording a solution of noninteracting NPs and polymers (Fig. 2A, step **2**). Moreover, we were pleased to find that the subsequent evaporation of $(NH_4)_2CO_3$ (in the form of CO_2 and NH_3; Fig. 2A) over the course of ~24 h results in the formation of well-defined colloidal crystals (Fig. 2A, step **3** and Fig. 2C–E).

With PAA$_{1800}$, the resulting crystals were highly faceted, with morphologies (e.g., icosahedra and hexagonal plates) characteristic of the face-centered cubic (fcc) structure, analogous to the same Au·TMA NPs cocrystallized with small-molecule oligoanions.[58] Moreover, high-resolution imaging revealed the presence of (111) and (100) facets, which are typical for the fcc structure[62] (Fig. 2C, right). The morphology of the crystals did not depend on the NP size (in the range tested; ~4.8–7.6 nm).

When the process was repeated with the longer polymer (PAA$_{100k}$), the NP crystals were less faceted and more rounded (Fig. 2D). This result can be understood by taking into consideration the relatively long length of PAA with a molecular weight of 100k (corresponding to ~1400 repeating units), namely, ~350 nm in its fully extended conformation (compared with only ~6.5 nm for the 1800 g/mol PAA). In order to maximize the contact with multiple Au·TMA NPs, the polymer chains fold and the ensemble assumes a more spherical shape, similarly to complex coacervates.[63–68] This trend continued with increasing polymer length: for PAA$_{450k}$, we observed the formation of pseudo-spherical aggregates (Fig. 2E), which, despite their shape, retained the crystalline order of the constituent NPs (Fig. 2E, right). Within these aggregates, each polymer interacts—on average—with ~15 NPs (assuming molecular weight of 450k, an NP size of 5 nm, and a complete deprotonation of PAA).

Interestingly, a more thorough inspection of the Au·TMA/PAA$_{450k}$ aggregates revealed the presence of multiple NP threads between neighboring colloidal crystals (Fig. 3). These threads appear to form as a result of the mechanical deformation of the aggregates during drying and/or sample preparation; they are composed of NPs deposited onto bundled polymer chains (see the low-contrast halo in Fig. 3F). The thicknesses of the threads ranged from ~10 NPs (Fig. 3C) down to individual NPs (Fig. 3B). No such threads were found with the two shorter polymers.

Having established that crystalline Au·TMA aggregates obtained from the long PAA are round, whereas those obtained from relatively short oligo- and polyanions are faceted, we hypothesized that the degree of faceting could be tuned by varying the molar ratio of a small to a large anion. To this end,
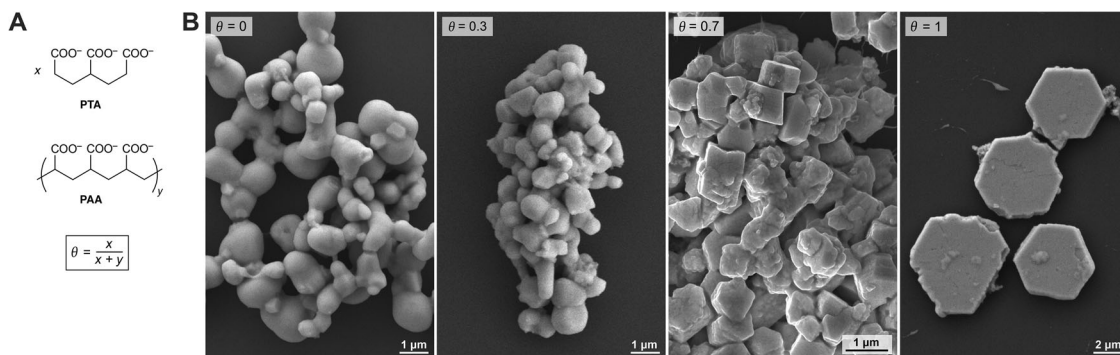
Figure 4. Tuning the morphology of crystalline aggregates of Au·TMA. (A) Structural similarity of pentane-1,3,5-tricarboxylic acid (PTA) and PAA, and the definition of θ. (B) SEM images of crystalline aggregates of Au·TMA. The higher the θ, the more faceted the crystals. For images of samples prepared at other values of θ, see Figure S2 (online only). All the samples were prepared from 6.34 ± 0.57 nm Au·TMA.

we worked with pentane-1,3,5-tricarboxylic acid (PTA; Fig. 4A)—a small molecule structurally similar to three consecutive repeating units of PAA. PTA was mixed with PAA_{450k} such that θ, defined as the ratio of PTA's COO^- groups to all the COO^- groups, was varied between 0 and 1 (Fig. 4A). The resulting mixture was added to 6.34 nm Au·TMA until no further changes in the UV/Vis spectra were observed. All PTA/PAA mixtures mediated the formation of amorphous NP aggregates, which were converted into crystalline ones via the $(NH_4)_2CO_3$ method (Fig. 2A). For $\theta = 0$ (i.e., pure PAA_{450k}), rounded crystalline aggregates were observed (Fig. 4B); the aggregates were larger and less uniform in size than the ones shown in Figure 2E as a result of a higher total concentration. As θ increased, the aggregates became more faceted, with regular hexagonal plates found for $\theta = 1$ (i.e., pure PTA, in agreement with previous findings[58]). The gradual faceting of Au·TMA/PAA/PTA aggregates (as opposed to changing the fraction of rounded versus faceted aggregates in a bimodal mixture) indicates that PAA and PTA interact with Au·TMA with similar propensities and that they coexist within the same aggregates.

To determine whether Au·TMA can also interact and cocrystallize with other polyanions, we worked with polyphosphoric acid (PPA; see Fig. 5 for the structural formula). The average degree of polymerization of the commercially available PPA[69] corresponds to ~22 (see the Materials and methods, online only)—similar to PAA_{1800} (degree of polymerization $\approx$ 25). Indeed, we found that
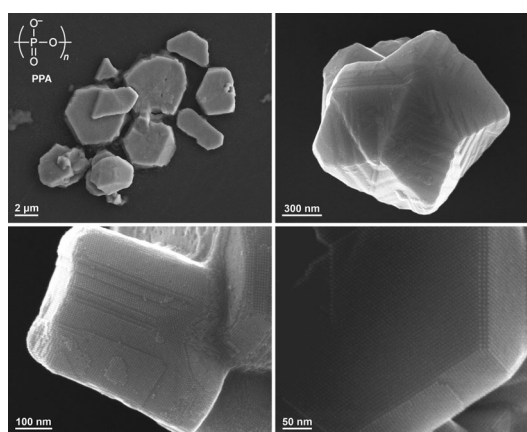

Figure 5. SEM images of crystalline assemblies of TMA-coated Au NPs and polyphosphoric acid (PPA) taken at increasing magnifications. The colloidal crystals were assembled from the same batch of PPA and Au·TMA of the following sizes, clockwise starting from top left: 4.84 ± 0.37 nm, 4.19 ± 0.35 nm, 5.78 ± 0.38 nm, and 5.37 ± 0.37 nm.

PPA can mediate attractive interactions between Au·TMA similarly to PAA; subsequent addition and spontaneous removal of $(NH_4)_2CO_3$ resulted in well-defined, faceted NP crystals similar to those obtained using PAA_{1800} (Fig. 5).

Next, we investigated whether crystalline NP assemblies could similarly be generated in a "reverse" system—that is, one incorporating negatively charged NPs and cationic polymers. To this end, we synthesized Au NPs functionalized with a single-component monolayer of sodium 11-mercaptoundecanesulfonate (MUS in Fig. 6A);
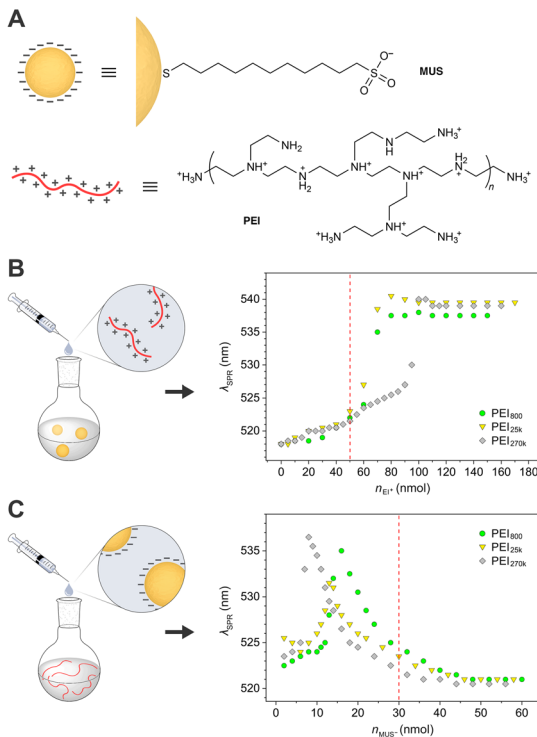
Figure 6. Aggregation of negatively charged nanoparticles with polycations. (A) Structural formulas of 11-mercaptoundecanesulfonate (MUS; counterion, Na$^+$) and protonated branched polyethylenimine (PEI; note: the polymer is branched and the structural formula is approximate; the degree of protonation is most likely not complete). (B) Changes in the position of the Au·MUS's SPR peak as a function of the amount of PEI added. The titrated solution contained 50 nmol of the NP-bound MUS groups. The amount of titrant added is expressed in terms of the number of ethylenimine (CH$_2$CH$_2$NH; EI) repeating units. The dashed red line denotes the theoretical point of neutrality (i.e., the number of MUS groups equalized by the number of EI units added). (C) Changes in the position of the Au·MUS's SPR peak as a function of the amount of Au·MUS added to the solution of PEI. The titrated solution contained a total of 30 nmol of the EI repeating units. The amount of titrant added is expressed in terms of the number of NP-bound MUS groups. The dashed red line denotes the theoretical point of neutrality (i.e., the number of EI units equalized by the number of NP-bound MUS groups added). The Au·MUS used in the titrations had a diameter of 6.34 ± 0.57 nm.

these NPs exhibited excellent solubility in water. For the polycation, we used commercially available branched polyethylenimine with three different degrees of polymerization: $M_w \approx 800$, $M_w \approx 25k$, and $M_w \approx 270k$, denoted as PEI$_{800}$, PEI$_{25k}$, and PEI$_{270k}$, respectively. Similar to PAA, the extent

of PEI protonation is pH-dependent, with low pH values favoring high densities of the electric charge. We note, however, that unlike for Au·TMA, the Au·MUS charge is not independent of pH; the protonation degree of the terminal sulfonate groups increases in acidic solutions. In other words, protonation of PEI at low pH values entails a partial loss of the negative charge on the NPs (the opposite is true for high pH values). The pK_b of PEI is ∼7; we, therefore, adjusted the pH of both solutions (Au·MUS and PEI) to ∼5.9 in order to ensure a high degree of PEI protonation while retaining Au·MUS largely deprotonated.

Figure 6B shows the results of titrating aqueous Au·MUS with solutions of PEIs. The two shorter PEIs exhibited a similar behavior, stabilizing the λ$_{SPR}$ of the NPs at ∼80 nmol of PEI (in terms of the number of EI units). For PEI$_{270k}$, a larger amount had to be added to achieve a plateau in the λ$_{SPR}$ (the gray markers in Fig. 6B); this result can be attributed to the branched structure of PEI, which makes the ammonium groups located deep inside the PEI molecule inaccessible for interaction with Au·MUS. Irrespective of the polymer length, the continued addition of PEI did not induce the disassembly of the Au·MUS/PEI aggregates.

An analogous trend was found upon reversing the order of titration: considerably less Au·MUS had to be added to PEI$_{270k}$ (compared with PEI$_{800}$ and PEI$_{25k}$) for NP aggregation to be observed (Fig. 6C, gray markers). Similar to Au·TMA (Fig. 1D), an excess of MUS-coated Au NPs induced the disassembly of the initial Au·MUS/PEI aggregates for all PEI lengths (Fig. 6C).

Working with the reverse system of Au·MUS and PEI, we also observed that the titration curves shifted from the expected behavior—although in directions opposite to those for Au·TMA/PAA. Namely, a larger than expected (based on the electroneutrality criterion, denoted by a dashed red line in Fig. 6B) amount of PEI had to be added to Au·MUS to induce aggregation; conversely, Au·MUS titrated into solutions of PEI aggregated faster than expected (markers versus the dashed red line in Fig. 6C). These results can be understood by taking into consideration the branched structure of PEI (which "screens" some of the ammonium groups) and/or an incomplete protonation of PEI's amine groups.
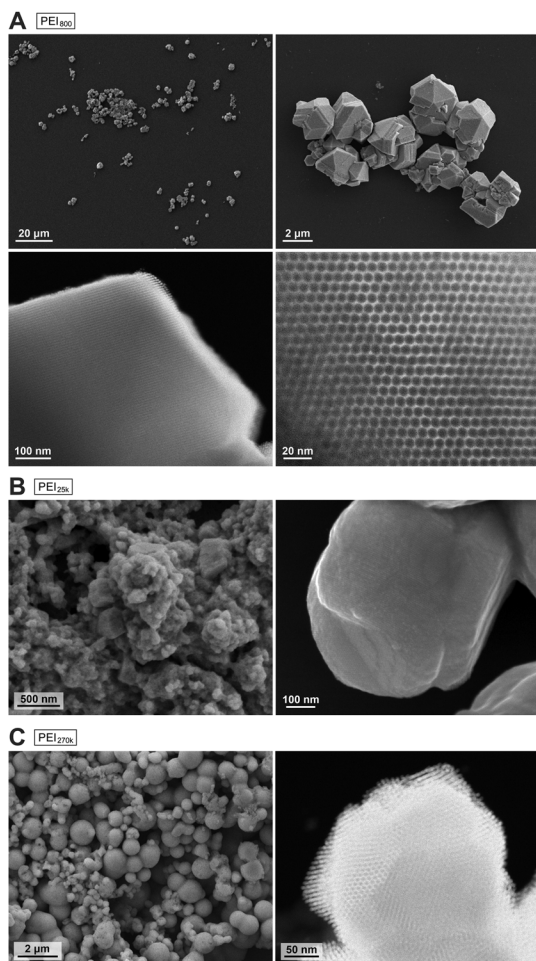
Figure 7. Crystalline assemblies of MUS-coated Au NPs and branched PEI. (A) SEM (top row) and HAADF-STEM (bottom row) images of crystalline assemblies obtained from Au·MUS and the shortest PEI (PEI$_{800}$). (B) SEM images of crystalline assemblies obtained from Au·MUS and medium-sized PEI (PEI$_{25k}$). (C) SEM (left) and HAADF-STEM (right) images of crystalline assemblies obtained from Au·MUS and the longest PEI (PEI$_{270k}$). All the samples were prepared from 6.34 ± 0.57 nm Au·TMA.

Finally, we attempted to fabricate colloidal crystals from Au·MUS and PEI. Upon the addition of a concentrated solution of $(NH_4)_2CO_3$, the Au·MUS/PEI aggregates disassembled for all the PEI batches (analogously to the Au·TMA/PAA aggregates; Fig. 2A). Then, we adjusted the pH of the solution to ∼5.9 in order to endow PEI and Au·MUS with a significant number of positive and negative charges, respectively. The spontaneous removal of $(NH_4)_2CO_3$ over the course of 24 h resulted in the

quantitative precipitation of the NPs from the solution in the form of colloidal crystals (Fig. 7). Interestingly, we observed the same dependence of crystal morphology on the polymer chain length as with Au·TMA/PAA: crystals mediated by PEI$_{800}$ were relatively large and strongly faceted (Fig. 7A); those obtained with PEI$_{25k}$ were crystalline but with less defined shapes (Fig. 7B); finally, aggregates made using PEI$_{270k}$ were mostly spherical (Fig. 7C, left), yet had a crystalline order of the NP building blocks (Fig. 7C, right).

Conclusions

In sum, we investigated the electrostatic interactions between charged Au nanospheres and oppositely charged polymers. Titrating the NPs with polymers resulted in the formation of amorphous NP/polymer composites that remained stable upon the continued addition of the polymer. By contrast, the addition of charged NPs to oppositely charged polymers resulted in the disassembly of the initially formed composites. The aggregates obtained by titrating NPs with polymers formed earlier than expected from the electroneutrality condition; this result suggests that, owing to their flexibility, the polymer chains can expose their charged residues more effectively than can the rigid inorganic nanospheres. The resulting amorphous NP/polymer aggregates could be transformed into crystalline ones by increasing and then slowly decreasing the ionic strength of the solution. The successful preparation of crystalline assemblies demonstrates that crystals from charged NPs can be obtained not only using oppositely charged small molecules,[58] but also polyions. The morphology of the resulting crystals was found to depend on the length of the polyion used. The crystals obtained using the shortest polymers (∼25 repeating charged units) were strongly faceted and indistinguishable from those obtained using oligoions.[58] The medium-sized polymers mediated the self-assembly of NPs into more rounded crystals, which exhibited some faceting. Finally, with the longest polymers, we observed the formation of pseudospherical assemblies, within which the crystalline order was still retained. This latter result is particularly interesting considering that the length of the longest polymer we worked with (PAA$_{450k}$) can be estimated, in its fully extended conformation, as ∼1.5 µm—well over two orders of magnitude

more than the typical NP size ($\sim$5 nm). Despite this large difference in size, colloidal crystals are observed, indicating that during the self-assembly process, the polymer chains fold in such a way that they accommodate the regular packing of NPs. Overall, these studies advance our understanding of nanoscale self-assembly and can pave the way toward obtaining composite materials with desired mechanical, plasmonic, and catalytic properties.

Acknowledgments

Author contributions

T.B. carried out the experimental work. R.K. wrote the manuscript with contributions from T.B.

Supporting information

Additional supporting information may be found in the online version of this article.

Figure S1. Sideview SEM images of crystalline assemblies obtained from TMA-functionalized 5.07 $\pm$ 0.41 nm Au NPs and PAA$_{450k}$.

Figure S2. Additional SEM images of crystalline aggregates of Au·TMA obtained using various mixtures of PAA$_{450k}$ and PTA.

Competing interests

The authors declare no competing interests.

References

1. Mirkin, C.A., R.L. Letsinger, R.C. Mucic & J.J. Storhoff. 1996. A DNA-based method for rationally assembling nanoparticles into macroscopic materials. *Nature* **382:** 607–609.
2. Grzelczak, M., J. Vermant, E.M. Furst & L.M. Liz-Marzán. 2010. Directed self-assembly of nanoparticles. *ACS Nano* **4:** 3591–3605.
3. Klajn, R., K.J.M. Bishop, M. Fialkowski, *et al.* 2007. Plastic and moldable metals by self-assembly of sticky nanoparticle aggregates. *Science* **316:** 261–264.
4. Santos, P.J., P.A. Gabrys, L.Z. Zornberg, *et al.* 2021. Macroscopic materials assembled from nanoparticle superlattices. *Nature* **591:** 586–591.
5. Shevchenko, E.V., D.V. Talapin, N.A. Kotov, *et al.* 2006. Structural diversity in binary nanoparticle superlattices. *Nature* **439:** 55–59.
6. Udayabhaskararao, T., T. Altantzis, L. Houben, *et al.* 2017. Tunable porous nanoallotropes prepared by post-assembly etching of binary nanoparticle superlattices. *Science* **358:** 514–518.
7. Macfarlane, R.J., B. Lee, M.R. Jones, *et al.* 2011. Nanoparticle superlattice engineering with DNA. *Science* **334:** 204–208.
8. Zhang, J., P.J. Santos, P.A. Gabrys, *et al.* 2016. Self-assembling nanocomposite tectons. *J. Am. Chem. Soc.* **138:** 16228–16231.
9. Grzelczak, M., L.M. Liz-Marzán & R. Klajn. 2019. Stimuli-responsive self-assembly of nanoparticles. *Chem. Soc. Rev.* **48:** 1342–1361.
10. Zhao, H., S. Sen, T. Udayabhaskararao, *et al.* 2016. Reversible trapping and reaction acceleration within dynamically self-assembling nanoflasks. *Nat. Nanotechnol.* **11:** 82–88.
11. Bian, T., Z. Chu & R. Klajn. 2020. The many ways to assemble nanoparticles using light. *Adv. Mater.* **32:** 1905866.
12. Samanta, D. & R. Klajn. 2016. Aqueous light-controlled self-assembly of nanoparticles. *Adv. Opt. Mater.* **4:** 1373–1377.
13. Balasubramaniam, S., N. Pothayee, Y. Lin, *et al.* 2011. Poly(*N*-isopropylacrylamide)-coated superparamagnetic iron oxide nanoparticles: relaxometric and fluorescence behavior correlate to temperature-dependent aggregation. *Chem. Mater.* **23:** 3348–3356.
14. Liu, Y., X. Han, L. He & Y. Yin. 2012. Thermoresponsive assembly of charged gold nanoparticles and their reversible tuning of plasmon coupling. *Angew. Chem. Int. Ed.* **51:** 6373–6377.
15. Sim, S., D. Miyajima, T. Niwa, *et al.* 2015. Tailoring micrometer-long high-integrity 1D array of superparamagnetic nanoparticles in a nanotubular protein jacket and its lateral magnetic assembling behavior. *J. Am. Chem. Soc.* **137:** 4658–4661.
16. Das, S., P. Ranjan, P.S. Maiti, *et al.* 2013. Dual-responsive nanoparticles and their self-assembly. *Adv. Mater.* **25:** 422–426.
17. Klajn, R., M.A. Olson, P.J. Wesson, *et al.* 2009. Dynamic hook-and-eye nanoparticle sponges. *Nat. Chem.* **1:** 733–738.
18. Chan, Y.-T., S. Li, C.N. Moorefield, *et al.* 2010. Self-assembly, disassembly, and reassembly of gold nanorods mediated by bis(terpyridine)-metal connectivity. *Chem. Eur. J.* **16:** 4164–4168.
19. Rao, A., S. Roy, M. Unnikrishnan, *et al.* 2016. Regulation of interparticle forces reveals controlled aggregation in charged nanoparticles. *Chem. Mater.* **28:** 2348–2355.
20. Heuser, T., A.-K. Steppert, C. Molano Lopez, *et al.* 2015. Generic concept to program the time domain of self-assemblies with a self-regulation mechanism. *Nano Lett.* **15:** 2213–2219.
21. Chen, S., C.X. Guo, Q. Zhao & X. Lu. 2014. One-pot synthesis of CO_2-responsive magnetic nanoparticles with switchable hydrophilicity. *Chem. Eur. J.* **20:** 14057–14062.
22. Lee, J.-W. & R. Klajn. 2015. Dual-responsive nanoparticles that aggregate under the simultaneous action of light and CO_2. *Chem. Commun.* **51:** 2036–2039.
23. Borsley, S. & E.R. Kay. 2016. Dynamic covalent assembly and disassembly of nanoparticle aggregates. *Chem. Commun.* **52:** 9117–9120.
24. Balazs, A.C., T. Emrick & T.P. Russell. 2006. Nanoparticle polymer composites: where two small worlds meet. *Science* **314:** 1107–1110.

25. Shenhar, R., T.B. Norsten & V.M. Rotello. 2005. Polymer-mediated nanoparticle assembly: structural control and applications. *Adv. Mater.* **17:** 657–669.

26. Yi, C., Y. Yang, B. Liu, *et al.* 2020. Polymer-guided assembly of inorganic nanoparticles. *Chem. Soc. Rev.* **49:** 465–508.

27. Berret, J.-F. 2011. Controlling electrostatic co-assembly using ion-containing copolymers: from surfactants to nanoparticles. *Adv. Colloid Interface Sci.* **167:** 38–48.

28. Boal, A.K., F. Ilhan, J.E. DeRouchey, *et al.* 2000. Self-assembly of nanoparticles into structured spherical and network aggregates. *Nature* **404:** 746–748.

29. Frankamp, B.L., O. Uzun, F. Ilhan, *et al.* 2002. Recognition-mediated assembly of nanoparticles into micellar structures with diblock copolymers. *J. Am. Chem. Soc.* **124:** 892–893.

30. Torii, Y., N. Sugimura, H. Mitomo, *et al.* 2017. pH-responsive coassembly of oligo(ethylene glycol)-coated gold nanoparticles with external anionic polymers via hydrogen bonding. *Langmuir* **33:** 5537–5544.

31. Ernenwein, D., P. Ghosh, V. Rotello & J. Chmielewski. 2010. Gold nanoparticle self-assembly promoted by a non-covalent, charge-complemented coiled-coil peptide. *J. Mater. Chem.* **20:** 5608–5611.

32. Kostiainen, M.A., P. Hiekkataipale, A. Laiho, *et al.* 2013. Electrostatic assembly of binary nanoparticle superlattices using protein cages. *Nat. Nanotechnol.* **8:** 52–56.

33. Liljeström, V., J. Mikkilä & M.A. Kostiainen. 2014. Self-assembly and modular functionalization of three-dimensional crystals from oppositely charged proteins. *Nat. Commun.* **5:** 4445.

34. De, M., O.R. Miranda, S. Rana & V.M. Rotello. 2009. Size and geometry dependent protein–nanoparticle self-assembly. *Chem. Commun.* 2157–2159.

35. Nakao, H., H. Shiigi, Y. Yamamoto, *et al.* 2003. Highly ordered assemblies of Au nanoparticles organized on DNA. *Nano Lett.* **3:** 1391–1394.

36. Ganguli, M., J. Venkatesh Babu & S. Maiti. 2004. Complex formation between cationically modified gold nanoparticles and DNA: an atomic force microscopic study. *Langmuir* **20:** 5165–5170.

37. Srivastava, S., B. Samanta, P. Arumugam, *et al.* 2007. DNA-mediated assembly of iron platinum (FePt) nanoparticles. *J. Mater. Chem.* **17:** 52–55.

38. Jang, S.G., A. Khan, C.J. Hawker & E.J. Kramer. 2012. Morphology evolution of PS-*b*-P2VP diblock copolymers via supramolecular assembly of hydroxylated gold nanoparticles. *Macromolecules* **45:** 1553–1561.

39. Liu, W., J. Mao, Y. Xue, *et al.* 2016. Nanoparticle loading induced morphological transitions and size fractionation of coassemblies from PS-*b*-PAA with quantum dots. *Langmuir* **32:** 7596–7605.

40. Zhao, J., C. Li & R. Liu. 2018. Enhanced oxygen reduction of multi-Fe$_3$O$_4$@carbon core–shell electrocatalysts through a nanoparticle/polymer co-assembly strategy. *Nanoscale* **10:** 5882–5887.

41. Ploshnik, E., A. Salant, U. Banin & R. Shenhar. 2010. Hierarchical surface patterns of nanorods obtained by co-assembly with block copolymers in ultrathin films. *Adv. Mater.* **22:** 2774–2779.

42. Warren, S.C., L.C. Messina, L.S. Slaughter, *et al.* 2008. Ordered mesoporous materials from metal nanoparticle–block copolymer self-assembly. *Science* **320:** 1748–1752.

43. Li, Z., K. Hur, H. Sai, *et al.* 2014. Linking experiment and theory for three-dimensional networked binary metal nanoparticle–triblock terpolymer superstructures. *Nat. Commun.* **5:** 3247.

44. Halevi, A., S. Halivni, M. Oded, *et al.* 2014. Co-assembly of A−B diblock copolymers with B'-type nanoparticles in thin films: effect of copolymer composition and nanoparticle shape. *Macromolecules* **47:** 3022–3032.

45. Kao, J., P. Bai, J.M. Lucas, *et al.* 2013. Size-dependent assemblies of nanoparticle mixtures in thin films. *J. Am. Chem. Soc.* **135:** 1680–1683.

46. Hsu, S.-W. & T. Xu. 2019. Tailoring co-assembly of nanodiscs and block copolymer-based supramolecules by manipulating interparticle interactions. *Macromolecules* **52:** 2833–2842.

47. Liu, Y., Y. Li, J. He, *et al.* 2014. Entropy-driven pattern formation of hybrid vesicular assemblies made from molecular and nanoparticle amphiphiles. *J. Am. Chem. Soc.* **136:** 2602–2610.

48. Lin, Y., V.K. Daga, E.R. Anderson, *et al.* 2011. Nanoparticle-driven assembly of block copolymers: a simple route to ordered hybrid materials. *J. Am. Chem. Soc.* **133:** 6513–6516.

49. Yan, N., Y. Zhang, Y. He, *et al.* 2017. Controllable location of inorganic nanoparticles on block copolymer self-assembled scaffolds by tailoring the entropy and enthalpy contributions. *Macromolecules* **50:** 6771–6778.

50. Sanwaria, S., A. Horechyy, D. Wolf, *et al.* 2014. Helical packing of nanoparticles confined in cylindrical domains of a self-assembled block copolymer structure. *Angew. Chem. Int. Ed.* **53:** 9090–9093.

51. Li, W., S. Liu, R. Deng & J. Zhu. 2011. Encapsulation of nanoparticles in block copolymer micellar aggregates by directed supramolecular assembly. *Angew. Chem. Int. Ed.* **50:** 5865–5868.

52. Caruso, F. & H. Möhwald. 1999. Preparation and characterization of ordered nanoparticle and polymer composite multilayers on colloids. *Langmuir* **15:** 8276–8281.

53. Srivastava, S. & N.A. Kotov. 2008. Composite layer-by-layer (LBL) assembly with inorganic nanoparticles and nanowires. *Acc. Chem. Res.* **41:** 1831–1841.

54. Li, Q., J.F. Quinn, Y. Wang & F. Caruso. 2006. Preparation of nanoporous polyelectrolyte multilayer films via nanoparticle templating. *Chem. Mater.* **18:** 5480–5485.

55. Li, L., R. Ma, Y. Ebina, *et al.* 2007. Layer-by-layer assembly and spontaneous flocculation of oppositely charged oxide and hydroxide nanosheets into inorganic sandwich layered materials. *J. Am. Chem. Soc.* **129:** 8000–8007.

56. Ai, H., M. Fang, S.A. Jones & Y.M. Lvov. 2002. Electrostatic layer-by-layer nanoassembly on biological microtempates: platelets. *Biomacromolecules* **3:** 560–564.

57. Ko, Y., H. Baek, Y. Kim, *et al.* 2013. Hydrophobic nanoparticle-based nanocomposite films using *in situ* ligand exchange layer-by-layer assembly and their nonvolatile memory applications. *ACS Nano* **7:** 143–153.

58. Bian, T., A. Gardin, J. Gemen, *et al.* 2021. Electrostatic co-assembly of nanoparticles with oppositely charged small molecules into static and dynamic superstructures. *Nat. Chem.* **13**, https://doi.org/10.1038/s41557-021-00752-9.

59. Peng, S., Y. Lee, C. Wang, *et al.* 2008. A facile synthesis of monodisperse Au nanoparticles and their catalysis of CO oxidation. *Nano Res.* **1:** 229–234.

60. Klajn, R., P.J. Wesson, K.J.M. Bishop & B.A. Grzybowski. 2009. Writing self-erasing images using metastable nanoparticle "inks". *Angew. Chem. Int. Ed.* **48:** 7035–7039.

61. Sawczyk, M. & R. Klajn. 2017. Out-of-equilibrium aggregates and coatings during seeded growth of metallic nanoparticles. *J. Am. Chem. Soc.* **139:** 17973–17978.

62. Lofton, C. & W. Sigmund. 2005. Mechanisms controlling crystal habits of gold and silver colloids. *Adv. Funct. Mater.* **15:** 1197–1208.

63. Tang, T.-Y.D., C.R.C. Hak, A.J. Thompson, *et al.* 2014. Fatty acid membrane assembly on coacervate microdroplets as a step towards a hybrid protocell model. *Nat. Chem.* **6:** 527–533.

64. Aumiller, W.M. & C.D. Keating. 2016. Phosphorylation-mediated RNA/peptide complex coacervation as a model for intracellular liquid organelles. *Nat. Chem.* **8:** 129–137.

65. Mason, A.F., B.C. Buddingh, D.S. Williams & J.C.M. van Hest. 2017. Hierarchical self-assembly of a copolymer-stabilized coacervate protocell. *J. Am. Chem. Soc.* **139:** 17309–17312.

66. Deng, N.-N. & W.T.S. Huck. 2017. Microfluidic formation of monodisperse coacervate organelles in liposomes. *Angew. Chem. Int. Ed.* **56:** 9736–9740.

67. Nakashima, K.K., J.F. Baaij & E. Spruijt. 2018. Reversible generation of coacervate droplets in an enzymatic network. *Soft Matter* **14:** 361–367.

68. Deng, J. & A. Walther. 2020. Programmable ATP-fueled DNA coacervates by transient liquid–liquid phase separation. *Chem* **6:** 3329–3343.

69. Platonov, V.A. 2000. Properties of polyphosphoric acid. *Fibre Chem.* **32:** 325–329.